Low-energy electron collisions with thioformaldehyde

Yong-Feng Wang and Shan Xi Tian*

Hefei National Laboratory for Physical Sciences at the Microscale and Department of Chemical Physics, University of Science and Technology of China, Hefei, Anhui 230026, China

(Received 22 June 2011; published 18 August 2011)

The elastic integral, differential, and momentum transfer cross sections and the excitation cross sections from the ground state to the first three low-lying electron excited states for low-energy (0–10 eV) electron collisions with thioformaldehyde (H_2CS) molecule are calculated using the R-matrix method. Eighteen target states are included in the close-coupling formalism. Three core-excited shape resonant states ($^2B_2$,$^2B_1$,$^2A_1$) and three Feshbach resonant states ($^2B_2$,$^2A_1$,$^2B_1$) are determined for the $(N+1)$-electron H_2CS^- system in the low-energy range. The dissociative electron attachment processes at the first two low-lying core-excited shape resonant states are proven by performing a series of scattering calculations, indicating the $S^-(^2P)$ yields together with the CH_2 fragment at three different states.

DOI: 10.1103/PhysRevA.84.022709 PACS number(s): 34.80.Bm

I. INTRODUCTION

Thioformaldehyde (H_2CS), which is the simplest molecule in the thiocarbonyl family, is well known to exist in interstellar clouds [1–3]. Recently, H_2CS was also detected for the first time in the circumstellar envelope around an asymptotic giant branch (AGB) star [4]. H_2CS plays an important role in the photochemical evolution of sulfur-containing species in atmospheric chemistry and astronomical systems [1–7]. Moreover, it is an important intermediate in organic synthesis [8,9], biological functions [10–12], and photochemical reactions [13–15].

Absorption spectra of H_2CS in the visible and ultraviolet regions have been investigated experimentally [16–21]. The lowest vibrational transition energies of $X\ ^1A_1$ to $A\ ^3A_2$ and $A\ ^1A_2$ ($n \rightarrow \pi^*$) were first determined to be 1.80 and 2.03 eV, respectively [16,17]; furthermore, the electron transitions to the higher valence $B\ ^1A_1$ ($\pi \rightarrow \pi^*$) and Rydberg states $C\ ^1B_2$ ($n \rightarrow 4s$), $D\ ^1A_1$ ($n \rightarrow 4p_y$), and $E\ ^1B_2$ ($n \rightarrow 4p_z$) were observed at 5.60, 5.84, 6.60, and 6.82 eV, respectively [18–20]. Recently, much more information on the valence to Rydberg state transitions was obtained [21,22]. Theoretically, there are a series of multireference configuration-interaction (MR-CI) studies on the spectroscopy of thioformaldehyde [23–28]. The experimental data of the basic properties of the ground-state H_2CS, such as ionization potential (IP), electron affinity (EA), and dipole moment (μ), are also available. The adiabatic IP ($V^a_{\rm ion}$) has been determined by the electron-impact mass spectrometry ($V^a_{\rm ion} = 9.44$ eV) [29] and by the photoionization mass spectrometry ($V^a_{\rm ion} = 9.376$ eV) [30]. The vertical IP ($V^v_{\rm ion}$) was obtained by the photoelectron spectroscopy ($V^v_{\rm ion} = 9.34$ eV [31], 9.38 eV [32]). The EA of H_2CS was measured to be 0.465 ± 0.023 eV by the photoelectron spectrum of the thioformaldehyde negative ion [33]. The μ value at the electronic ground state is 1.6491 D, determined by the molecular-beam electric resonance technique [34], and 1.647 D, determined by microwave spectroscopy [35]. To the best of our knowledge, there have been no reports up to now on the electron-impact spectroscopy of H_2CS. In the electron collisions with this molecule, the electron transitions including the spin-permitted and spin-forbidden promotions can be observed. Meanwhile, it is worth exploring the coupling mechanism between the electron-molecule resonant states formed in the collisions and the electron-attachment-induced dissociations.

In the present work, the integral elastic and inelastic cross sections of the low-energy (0–10 eV) electron scattering from H_2CS are calculated using the UK polyatomic R-matrix codes [36,37]. High efficiency and the accurate treatment of the electron multiconfigurations guarantee the successful applications of the R-matrix method in a series of studies on the small radicals [38] and polyatomic molecules [39,40]. The electron-scattering calculations for H_2CS are performed within the CI scheme and the close-coupling approximation. Here we are interested in the low-energy region ($\leqslant$10 eV) because in this energy range the transient-state negative ion, also known as the electron-molecule resonant states, can be formed in the different mechanisms, i.e., the incoming electron can occupy one of the unoccupied molecular orbitals (MOs) or excite any of the occupied MOs as it falls into another one. The electron-molecule resonant states are usually shorted-lived and decay into energetically open channels, e.g., dissociation to a negative ion and a neutral fragment. The excitation cross sections from the molecular ground state to a few low-lying excited states have also been calculated, and these excited states formed in the inelastic collisions can decay into the ground state with photon emissions or by coupling with the dissociation channels to produce the anionic and neutral fragments. Furthermore, the POLYDCS code [41] is employed for the calculations of rotationally elastic and inelastic differential cross sections (DCSs) in which the K-matrix elements are required and obtained within the 18-state R-matrix approximation.

II. THEORETICAL METHOD

The R-matrix method has been described in detail elsewhere [42,43]. In a fixed nuclei R-matrix approach, the configuration space is divided into an inner region and an outer region. The inner region is defined as the volume of a sphere centered at the center of mass of the target molecule. This region is

*sxtian@ustc.edu.cn

treated in varieties, but ensuring that the charge density of the target is fully constrained in this region. In the inner region, the scattering electron is indistinguishable from the electrons of the target, and the electron-electron correlation and exchange are strong. The highly qualified electron wave functions are required in the scattering calculations. In the outer region, it is assumed that the scattering electron can be considered to be distinct. This electron, therefore, moves in a local potential arising from its long-range interaction with the target. The electron exchange and correlation effects between the scattering electron and target electrons are neglected.

In the inner region, the wave function of the $(N+1)$-electron system is expanded in the following way:

$$\Psi_k^{N+1} = A\sum_{ij} a_{ijk}\Phi_i^N(x_1,\ldots,x_N)u_{ij}(x_{N+1}) + \sum_i b_{ik}\chi_i^{N+1}(x_1,\ldots,x_{N+1}), \quad (1)$$

where A is an antisymmetrization operator, x_N is the spatial and spin coordinates of the Nth electron, ${\Phi_i}^N$ is the ith target wave function, and u_{ij} is a continuum orbital describing the scattering electron. The target wave function ${\Phi_i}^N$ is represented using the complete active space CI (CASCI) model, which ensures a good balance between the N-electron target and the $(N+1)$-electron wave functions. The sum in the second term of Eq. (1) represents the short-range correlation and polarization effects, running over configurations ${\chi_i}^{N+1}$ that are known as L^2 functions. These ${\chi_i}^{N+1}$ are multicenter quadratically integrable functions constructed, as the target wave functions, with the target occupied and virtual MOs. a_{ijk} and b_{ik} are the variational coefficients obtained by diagonalizing the $(N+1)$ Hamiltonian.

The configurations included in the CI expansion are generated as the products of MOs; the same set of orbitals must be used for all electronic states. In the polyatomic R-matrix suite, both the molecular MOs and the continuum orbitals are expanded in terms of Gaussian-type orbitals (GTOs). The basis functions for the MOs, centered on each nucleus, are adapted from a standard quantum chemistry basis set. The continuum basis functions are centered at the center of mass of the target. First, the Schmidt orthogonalization procedure is used to orthogonalize target and continuum MOs, then Löwdin symmetric orthogonalization is used to orthogonalize the continuum orbitals among themselves and remove linearly dependent functions [36,44].

III. TARGET AND SCATTERING MODELS

The molecule H_2CS, which belongs to the C_{2v} point group, is a closed-shell system. The geometrical parameters at the ground state $X\ {}^1A_1$ are experimentally determined as $R(C=S)=1.611$ Å, $R(C\text{-}H)=1.093$ Å, and bond angle $(H\text{-}C\text{-}H)=116.9^\circ$ [45], and are used in the present calculations. We use the double-ζ plus polarization (DZP) Gaussian basis set contracted as $(9s5p1d)/(4s2p1d)$ for the C atom, $(12s8p1d)/(6s4p1d)$ for the S atom [46], and $(8s2p)/(5s2p)$ for the H atom [47]. We have not used the larger basis set augmented with more diffuse functions since the electron wave function could extend outside the inner region (radius $\sim 12a_0$). First, a self-consistent-field (SCF) calculation for the ground-state target is performed, and a set of occupied and virtual MOs are obtained. The Hartree-Fock electron configuration at the ground state is $1a_1{}^2 2a_1{}^2 3a_1{}^2 4a_1{}^2 1b_1{}^2 1b_2{}^2 5a_1{}^2 6a_1{}^2 2b_2{}^2 7a_1{}^2 2b_1{}^2 3b_2{}^2$. The SCF energy for the ground state of H_2CS is -436.5129 hartree, and the energies of the higher occupied MOs with the irreducible representations $7a_1$, $2b_1$, and $3b_2$ are -14.66, -11.27, and -9.50 eV, respectively. The eigenvalues of the first three virtual MOs $3b_1$, $8a_1$, and $4b_2$ are 1.36, 3.01, and 3.81 eV, respectively. Within Koopmans' theorem, the first $V_{\rm ion}^v$ is simply estimated to be 9.50 eV, which is in agreement with the experimental value (9.38 eV) [32]. To improve the calculations of the ground and excited states, the CASCI model is employed. In the present CASCI calculations, we keep 14 electrons frozen in the inner MOs $1a_1$, $2a_1$, $3a_1$, $4a_1$, $1b_1$, $1b_2$, and $5a_1$, while allowing the remaining 10 electrons to occupy freely the outer MOs $6a_1$, $2b_2$, $7a_1$, $2b_1$, $3b_2$, $3b_1$, $8a_1$, $4b_2$, and $9a_1$ (the latter four are the virtual MOs of the ground-state target). The CASCI energy of the ground state is -436.5407 hartree. The dipole moment and quadrupole moments have also been calculated to provide additional information on the charge distribution in the H_2CS molecule. The μ value at the ground state is predicted to be 1.7979 D, in good agreement with the experimental datum of 1.6491 D [34]. The quadrupole components Q_{20} and Q_{22} at the ground state are 2.013 258 and 0.083 765 a.u., respectively. Furthermore, the rotational constants are 9.6399, 0.5915, and 0.5573 $\rm cm^{-1}$.

In the CASCI calculations of the $(N+1)$-electron system, no R-matrix poles are found to have energies lower than the ground state $X\ {}^1A_1$, implying that there is no bound state of the anion H_2CS^-. In the experiment, however, H_2CS^- can be formed at a bound state [32]. Since the geometry of the ground-state H_2CS^- [32,48], also in the C_{2v} point group, is slightly different from that of H_2CS, the EA of H_2CS should be positive, 0.465 ± 0.023 eV [32]. The existence of such a bound state could seriously influence the cross sections at the corresponding symmetry, ${}^2B_1$, of the bound-state H_2CS^-. In this work, the SCF calculations for the ground-state $({}^2B_1)$ H_2CS^- at the H_2CS equilibrium geometry have been performed. The energy of the singly occupied MO (SOMO) $3b_1$ is -0.20 eV. The EA of 0.20 eV can be simply estimated within Koopmans' theorem, which is close to the experimental result [32]. Furthermore, using the SCF wave functions of H_2CS^-, the CASCI calculations predict a pole of ${}^2B_1$ symmetry that is 0.11 eV lower than the ground-state energy of H_2CS. Therefore, this ${}^2B_1$-state anion H_2CS^- is a bound state, in accord with the experimental result [32]. In the present calculations, the SCF orbitals of H_2CS^- are only used for the calculations of the elastic cross section for ${}^2B_1$ symmetry, while the SCF orbitals of H_2CS are used for the other calculations.

The predominant configurations, the transition moments, the number of configuration state functions (CSFs), and the vertical excitation energies of the target state are listed in Table I. The vertical excitation energies for the first three excited states are in good agreement with the MR-CI results [23–26], while the deviations become distinct for the higher states. These differences may arise from the different basis sets or sizes of the active space used in the respective calculations.

TABLE I. Predominant configuration, transition moment (in a.u.), the number of configuration-state functions (N), and the vertical excitation energies (in eV) for the target states of H_2CS.

State	Dominant configuration	Transition moment	N	Vertical excitation energies					
				This work	MR-CI[a]	MR-CI[b]	MR-CI[c]	MR-CI[d]	Expt.
$1\,^1A_1$	$\cdots 6a_1^2 2b_2^2 7a_1^2 2b_1^2 3b_2^2$		1408	0.00	0.00	0.00	0.00	0.00	
$1\,^3A_2$	$\cdots 6a_1^2 2b_2^2 7a_1^2 2b_1^2 3b_2^1 3b_1^1$		1892	2.37	1.84	2.22		2.14	1.80[e]
$1\,^1A_2$	$\cdots 6a_1^2 2b_2^2 7a_1^2 2b_1^2 3b_2^1 3b_1^1$		1268	2.66	2.17	2.38	2.40		2.03[f]
$1\,^3A_1$	$\cdots 6a_1^2 2b_2^2 7a_1^2 2b_1^1 3b_2^2 3b_1^1$		1868	3.57	3.28	3.56		3.74	
$1\,^3B_2$	$\cdots 6a_1^2 2b_2^2 7a_1^2 2b_1^2 3b_2^1 8a_1^1$		1912	6.80	5.72	5.91		5.68	
$1\,^3B_1$	$\cdots 6a_1^2 2b_2^2 7a_1^1 2b_1^2 3b_2^2 3b_1^1$		1888	6.87	6.38			6.32	
$1\,^1B_2$	$\cdots 6a_1^2 2b_2^2 7a_1^2 2b_1^2 3b_2^1 8a_1^1$	−0.0805	1336	6.95	5.83	5.95	5.76		5.84[g]
									5.845[h]
$1\,^1B_1$	$\cdots 6a_1^2 2b_2^2 7a_1^1 2b_1^2 3b_2^2 3b_1^1$	−0.3587	1280	7.86	7.51	7.17	7.31		
$2\,^3A_1$			1868	8.08	6.58	6.71		6.53	
$2\,^1A_1$		−0.0040	1408	8.11	6.62	6.80	6.56		6.60[g]
									6.837[h]
$3\,^1A_1$		0.0204	1408	8.24			6.88		
$2\,^3A_2$			1892	8.46	7.79	6.90		6.56	
$4\,^1A_1$		−0.0216	1408	8.63	7.92	7.02	7.37		5.60[g]
									6.132[h]
$2\,^1A_2$			1268	8.81	7.88	6.92	6.74		
$2\,^3B_1$			1888	9.15				7.53	
$2\,^1B_1$		−0.6937	1280	9.35			7.57		
$2\,^3B_2$			1912	9.75				6.38	
$2\,^1B_2$		0.2482	1336	10.12			6.54		6.82[g]
									6.586[h]

[a]From Ref. [23].
[b]From Ref. [24].
[c]From Ref. [25].
[d]From Ref. [26].
[e]From Ref. [17].
[f]From Ref. [16].
[g]From Ref. [20].
[h]From Ref. [21].

The energies of the first two excited states are 0.57 and 0.63 eV larger than the experimental values [16,17], respectively. Furthermore, for the higher excited states, our results are also larger than the MR-CI [23–26] and experimental results [20,21].

In the present scattering calculations, 18 target states given in Table I are included in the close-coupling expansion, in which four states are in $^1A_1$ symmetry and each two is in $^3A_1$, $^1B_1$, $^3B_1$, $^1B_2$, $^3B_2$,$^1A_2$, and $^3A_2$ symmetries, respectively. Our scattering calculations are performed for doublet spin scattering states with A_1, B_1, B_2, and A_2 symmetries. The continuum orbitals up to g-partial waves (the quantum number $l \leqslant 4$) are orthogonalized to the target orbitals based on the mixture of Schmidt and Löwdin symmetric orthogonalization and represented by GTOs centered at the molecular center of gravity [49]. The continuum orbitals with an overlap of less than 2×10^{-17} are removed [36]. The quantity balance between the correlation included in the target states and that in the scattering calculation is achieved by allowing 11 electrons (10 valance electrons plus one scattering electron) to move freely among $6a_1$, $2b_2$, $7a_1$, $2b_1$, $3b_2$, $3b_1$, $8a_1$, $4b_2$, and $9a_1$ MOs.

IV. RESULTS

A. Elastic and inelastic total cross sections

The elastic cross section of electron collision with H_2CS in an 18-state approach is shown in Fig. 1. As mentioned above, the first $^2B_1$ state of the anion H_2CS^- is a bound state [32]. The elastic cross section is also examined for B_1 symmetry with a static-exchange (SE) approach and a one-state CI calculation, which is shown as the inside panel of Fig. 1. One broad peak at 1.94 eV is found in the elastic cross-section profile obtained with the SE calculation, while a narrow peak is observed at 0.47 eV in the one-state CI calculation. However, this peak (or resonance) is not real because it disappears in the 18-state CI calculation. This artificial resonant state should be converted into the bound state as described in Sec. III due to the proper treatment of the polarization effects by the more states involved in the scattering calculations. The retention of a large number of coupling channels in the 18-state model provides the necessary polarization potential in an *ab initio* way, which is crucial for determining the true resonances and their resonance parameters. In Fig. 1, the contribution of $^2A_1$ symmetry is much larger than those

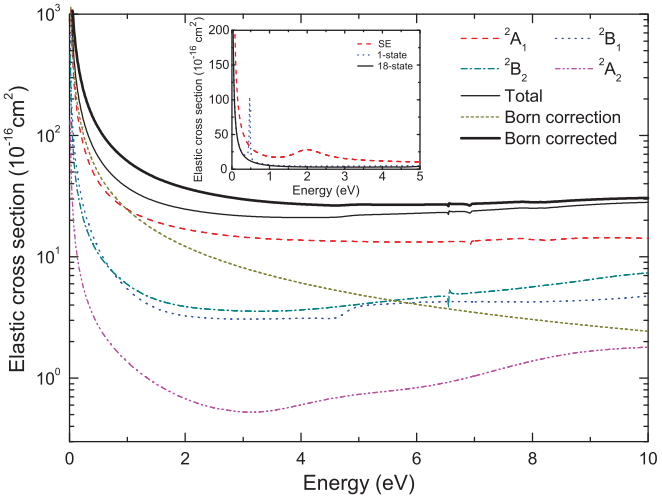

FIG. 1. (Color online) Elastic cross section of the electron collision with H_2CS. Dashed curve: $^2A_1$; dotted curve: $^2B_1$; dash-dotted curve: $^2B_2$; single-dash-double-dotted curve: $^2A_2$; thin solid curve: total; short-dashed curve: Born correction; thick solid curve: Born-corrected. Inside panel: elastic cross sections for $^2B_1$ symmetry with static-exchange (SE) (dashed line), 1-state (dotted line), and 18-state (solid line) CI calculations in the energy range of 0–5 eV.

of $^2B_1$ and $^2B_2$ symmetries, while the contribution of $^2A_2$ symmetry is the smallest. The contributions of $^2B_1$ and $^2B_2$ symmetries are comparable to each other over the whole energy range investigated in this work. Due to the long-range dipole interaction, the DCS is singular in the forward direction and therefore the elastic cross section is formally divergent in the fixed-nuclei approximation. In order to obtain a converged elastic cross section, the effect of molecular rotation must be included along with a very large number of partial waves. Therefore, in the present calculations, the contribution of partial waves with $l \geqslant 5$ to the elastic cross section is considered using the first Born approximation [50,51]. As shown in Fig. 1, the contribution of Born correction is larger than the contributions of $^2B_1$, $^2B_2$, and $^2A_2$ symmetries below about 5.5 eV, even exceeding the contribution of $^2A_1$ symmetry at energies less than 1.0 eV. Furthermore, there are two small dips around 6.55 and 6.94 eV in the total elastic cross section. Carefully inspecting the four components of the total elastic cross section, we find that the resonances around 6.55 and 6.94 eV come from $^2B_2$ and $^2A_1$ symmetries, respectively. The resonances in multichannel scattering are characterized not only by the structures exhibited in the cross-section curves, but also, more importantly, by the sudden jumps of the eigenphase sum for π radians. In most cases, the position and width of a true resonance can be determined by fitting the eigenphase sum to a Breit-Winger form [52],

$$\delta(E) = \delta_0(E) - \tan^{-1}\left(\frac{\Gamma/2}{E_r - E}\right), \tag{2}$$

where E_r is the resonance position, Γ is the width, and $\delta_0(E)$ is the background phase near the resonance. When the background varies slowly over the resonance profile, Γ can be determined from the relation [53]

$$\Gamma = 2/\delta'(E_r). \tag{3}$$

In general, the point of maximum gradient $\delta'(E)$ serves as definitions for the position of the resonance, and the width can be determined using Eq. (3). Through analyzing the eigenphase sums calculated with the 18-state model, the energy positions and widths of resonances together with their parent states are obtained (see Table II). The dip at 6.55 eV in $^2B_2$ symmetry has a width of 0.0189 eV and is a Feshbach resonance whose parent state is $1\ ^3B_2$ state of H_2CS. The configuration of this Feshbach resonance is $\ldots 6a_1^2 2b_2^2 7a_1^2 2b_1^2 3b_2^1 8a_1^2$. The dip at 6.94 eV in $^2A_1$ symmetry is also a Feshbach resonance with a width of 0.0304 eV, and its parent state is $1\ ^1B_2$ state. The configuration of the second Feshbach resonance is $\ldots 6a_1^2 2b_2^2 7a_1^2 2b_1^2 3b_2^1 8a_1^1 4b_2^1$. The parent states and the configurations of resonances are determined by performing a set of calculations including some carefully chosen configurations and by manipulating the active space of calculations.

The excitation cross sections of the transitions from the ground state $X\ ^1A_1$ to the first three excited states $1\ ^3A_2$, $1\ ^1A_2$, and $1\ ^3A_1$ are depicted in Figs. 2, 3, and 4, respectively. It is noted that the former two transitions are electric-dipole-forbidden and the last one is spin-forbidden. Figure 2 shows the $X\ ^1A_1 \rightarrow 1\ ^3A_2$ excitation cross section together with the individual contribution of the different scattering symmetry. Except for some specific points, the contribution of $^2B_1$ symmetry is much larger than that of any other symmetry. The total excitation cross section shows a sharp peak at 6.55 eV, a small peak at 6.94 eV, a diffuse peak at 5.15 eV, a shoulder at 3.62 eV, and a small dip at 9.05 eV. By meticulous examinations of each contribution of four scattering symmetries, we find that the resonances around 3.62 and 6.55 eV come from $^2B_2$ scattering symmetry (see the inside panel of Fig. 1), the resonances around 5.15 and 9.05 eV are attributed to $^2B_1$ scattering symmetry, and the resonance at

TABLE II. Resonant states of the electron-H_2CS scattering system.

State	Designation of resonance	Type of resonance	Resonance parameters (eV)		Parent state (eV)	
			Position/E_r	Width/Γ	State	Position
$^2B_2$	$\cdots 6a_1^2 2b_2^2 7a_1^2 2b_1^2 3b_2^1 3b_1^2$	core-excited	3.62	0.5698	$1\ ^3A_2$	2.37
$^2B_1$	$\cdots 6a_1^2 2b_2^2 7a_1^2 2b_1^1 3b_2^2 3b_1^2$	core-excited	5.15	1.1696	$1\ ^3A_1$	3.57
$^2B_2$	$\cdots 6a_1^2 2b_2^2 7a_1^2 2b_1^2 3b_2^1 8a_1^2$	Feshbach	6.55	0.0189	$1\ ^3B_2$	6.80
$^2A_1$	$\cdots 6a_1^2 2b_2^2 7a_1^2 2b_1^2 3b_2^1 8a_1^1 4b_2^1$	Feshbach	6.94	0.0304	$1\ ^1B_2$	6.95
$^2A_1$	$\cdots 6a_1^2 2b_2^2 7a_1^1 2b_1^2 3b_2^2 3b_1^2$	core-excited	7.98	0.0370	$1\ ^3B_1$	6.87
$^2B_1$	$\cdots 6a_1^2 2b_2^2 7a_1^2 2b_1^1 3b_2^2 8a_1^2$	Feshbach	9.05	0.0241	$2\ ^3B_1$	9.15

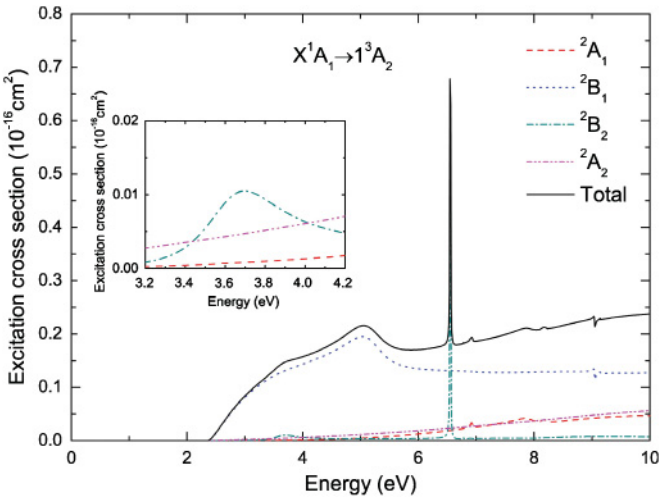

FIG. 2. (Color online) Electron-impact excitation cross sections from the ground state $X\ ^1A_1$ to the $1\ ^3A_2$ state. Dashed curve: $^2A_1$ contribution; dotted curve: $^2B_1$ contribution; dash-dotted curve: $^2B_2$ contribution; single-dash-double-dotted curve: $^2A_2$ contribution; solid curve: total. Inset: the enlargement for the energy region of 3.2–4.2 eV.

6.94 eV is due to $^2A_1$ scattering symmetry. The peaks around 6.55 and 6.94 eV arise from the Feshbach resonances that have been found in the elastic cross-section calculations. The additional calculations indicate that the shoulder around 3.62 eV corresponds to a core-excited shape resonance $^2B_2$ with a width of 0.5698 eV. The parent state of this core-excited resonance is $1\ ^3A_2$ and the configuration is $\ldots 6a_1^2 2b_2^2 7a_1^2 2b_1^2 3b_2^1 3b_1^2$. The diffuse peak at 5.15 eV is related to a core-excited shape resonance $^2B_1$ with a width of 1.1696 eV and a configuration as $\ldots 6a_1^2 2b_2^2 7a_1^2 2b_1^1 3b_2^2 3b_1^2$. It can decay to its parent state $1\ ^3A_1$ if the electron of $3b_1$ is detached. The dip around 9.05 eV is attributed to a Feshbach resonance

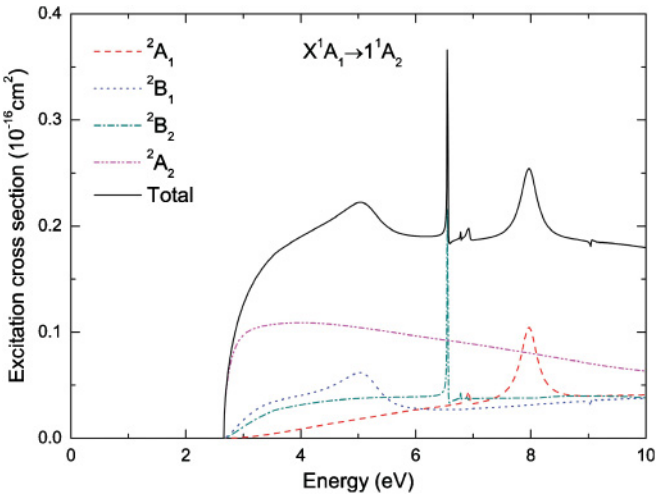

FIG. 3. (Color online) Electron-impact excitation cross sections from the ground state $X\ ^1A_1$ to the $1\ ^1A_2$ state. Dashed curve: $^2A_1$ contribution; dotted curve: $^2B_1$ contribution; dash-dotted curve: $^2B_2$ contribution; single-dash-double-dotted curve: $^2A_2$ contribution; solid curve: total.

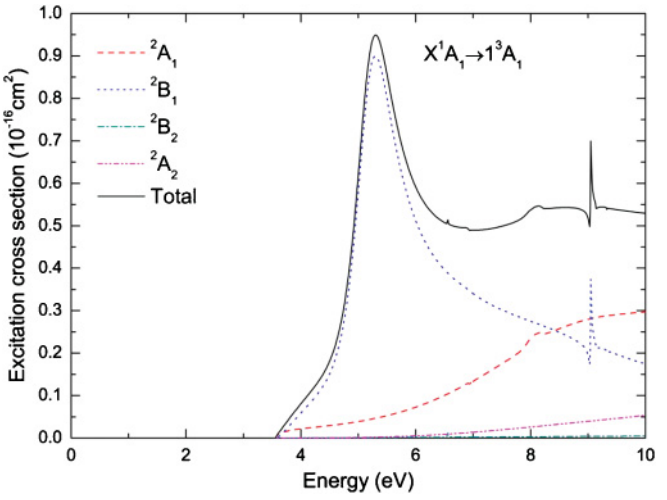

FIG. 4. (Color online) Electron-impact excitation cross sections from the ground state $X\ ^1A_1$ to the $1\ ^3A_1$ state. Dashed curve: $^2A_1$ contribution; dotted curve: $^2B_1$ contribution; dash-dotted curve: $^2B_2$ contribution; single-dash-double-dotted curve: $^2A_2$ contribution; solid curve: total.

$^2B_1$ with a width of 0.0241 eV and a configuration of $\ldots 6a_1^2 2b_2^2 7a_1^2 2b_1^1 3b_2^2 8a_1^2$. Its parent state is $2\ ^3B_1$.

The excitation cross sections of the $X\ ^1A_1 \rightarrow 1\ ^1A_2$ transition are plotted in Fig. 3. Here we also observe several resonances. The sharp peak in $^2B_2$ symmetry at 6.55 eV and the small peak in $^2A_1$ symmetry at 6.94 eV have been detected both in the elastic-scattering process and the $X\ ^1A_1 \rightarrow 1\ ^3A_2$ transition. The diffuse peak around 5.15 eV and the dip at 9.05 eV attributing to $^2B_1$ symmetry are also found in Fig. 2. An additional strong peak at 7.98 eV is observed in Fig. 3, which is due to $^2A_1$ symmetry scattering. This $^2A_1$ symmetry resonance is further proven to be a core-excited shape resonant state with a width of 0.0370 eV, and its configuration is $\ldots 6a_1^2 2b_2^2 7a_1^1 2b_1^2 3b_2^2 3b_1^2$ and can decay into the parent state $1\ ^3B_1$ after the electron detachment from $3b_1$ MO. The $X\ ^1A_1 \rightarrow 1\ ^3A_1$ excitation cross sections are shown in Fig. 4. The predominant contribution in the lower-energy range is of $^2B_1$ symmetry, indicating an extremely high peak at about 5.15 eV. The significant enhancement of the cross section arises from the electron collision energy approaching the threshold of this $^2B_1$ core-excited shape resonance. At the higher energy, the $^2B_1$ symmetry Feshbach state leads to a remarkable resonant peak around 9.05 eV. Although this resonance has been observed in the $X\ ^1A_1 \rightarrow 1\ ^3A_2$ and $X\ ^1A_1 \rightarrow 1\ ^1A_2$ transitions, it is observed much more clearly in the present $X\ ^1A_1 \rightarrow 1\ ^3A_1$ process.

B. Differential cross section

The calculation of the DCSs provides a more stringent test for any theoretical model. The DCS for a general polyatomic molecule is given by

$$\frac{d\sigma}{d\Omega} = \sum_L A_L P_L(\cos\theta), \tag{4}$$

where P_L is a Legendre function. The A_L coefficients have been discussed in detail by Gianturco and Jain [54]. For a

polar molecule, this expansion over L converges slowly. The following closure formula is used to accelerate the convergence of DCS:

$$\frac{d\sigma}{d\Omega} = \frac{d\sigma^B}{d\Omega} + \sum_L \left(A_L - A_L^B\right) P_L(\cos\theta). \quad (5)$$

The superscript B represents the relevant quantity, which is calculated in the Born approximation with an electron–point-dipole interaction. The convergence of the summation over L in (5) is now rapid because the contribution from the higher partial waves to the DCS is dominated by the electron-dipole interaction. The quantity $d\sigma^B/d\Omega$ for any initial rotor state $|J\tau\rangle$ is given by the sum over all the final rotor states $|J'\tau'\rangle$,

$$\frac{d\sigma^B}{d\Omega} = \sum_{J'\tau'} \frac{d\sigma^B}{d\Omega}\left(J\tau \to J'\tau'\right). \quad (6)$$

The expressions for the state-to-state rotationally inelastic DCS, $d\sigma^B/d\Omega(J\tau \to J'\tau')$, for a spherical top, a symmetric top, and asymmetric top molecules have been given by Sanna and Gianturco [41]. The maximum value of l_B in the Born K matrices is 30. The value of L in the Legendre expansion of the calculated A_L coefficients is 18. The calculated dipole moment (1.7979 D) and rotational constants ($A = 9.6399\ \text{cm}^{-1}$, $B = 0.5915\ \text{cm}^{-1}$, and $C = 0.5573\ \text{cm}^{-1}$) for H_2CS are used in the calculations of the elastic ($J = 0 \to J' = 0$) and rotationally inelastic ($J = 0 \to J' = 1, 2, 3, \ldots$) DCSs.

Our calculated rotationally resolved DCSs at the electron collision energy of 2 eV are shown in Fig. 5. The calculated DCS is converged when J' increases up to 5. The elastic and inelastic ($J = 0 \to J' = 1$) contributions are the main contributions to the total DCS. The contribution of the higher J' decreases when J' increases. The component ($J = 0 \to J' = 1$) is comparable to the elastic component ($J = 0 \to J' = 0$) at higher angles, but exceeds the latter when the angle is smaller than 35°. This may be due to the large dipole moment of

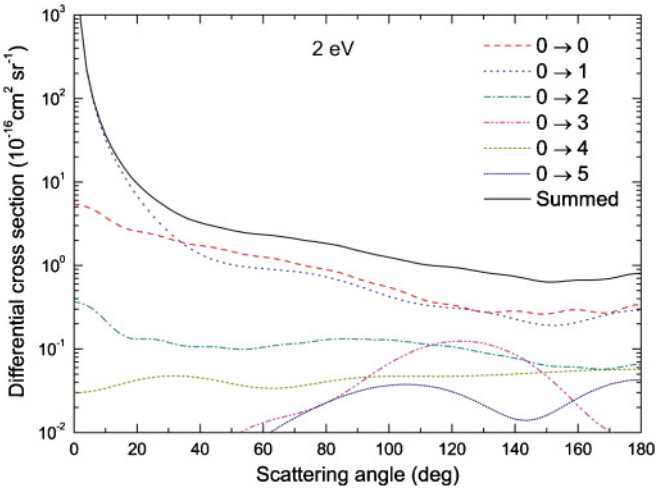

FIG. 5. (Color online) Electron impact R-matrix rotationally resolved state-to-state ($J \to J'$) differential cross sections of H_2CS at 2 eV. Dashed curve: $J = 0 \to J' = 0$; dotted curve: $J = 0 \to J' = 1$; dash-dotted curve: $J = 0 \to J' = 2$; single-dash-double-dotted curve: $J = 0 \to J' = 3$; short-dashed curve: $J = 0 \to J' = 4$; short-dotted curve: $J = 0 \to J' = 5$; solid curve: summed.

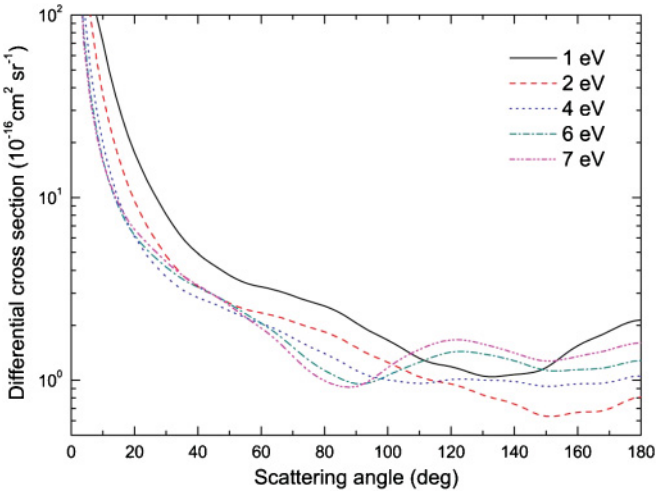

FIG. 6. (Color online) Differential cross sections at 1, 2, 4, 6, and 7 eV. Solid curve: 1 eV; dashed curve: 2 eV; dotted curve: 4 eV; dash-dotted curve: 6 eV; single-dash-double-dotted curve: 7 eV.

H_2CS. The DCSs obtained by summarizing the rotational cross sections for ($J = 0 \to J' = 0$–5) at the selected energies of 1, 2, 4, 6, and 7 eV are depicted in Fig. 6. The DCSs at all the impact energies show sharp increases at the smaller scattering angles due to the dipolar nature of the target. Such a backward-scattering preference is also observed for the similar dipolar target H_2CO [40]. As shown in Fig. 6, the DCSs at 1 and 2 eV show minima at about 130° and 150° respectively. When the incident energy increases to 4 eV, there are two minima, one at about 110° and the other at 150°. At incident energies of 6 and 7 eV, the first minimum of the DCS shifts to the smaller angle of about 90°.

In Fig. 7, the momentum transfer cross sections (MTCSs) are presented in the energy range of 0–8 eV. The MTCS indicates the weights of backward scattering and it is an important measure in a warm study of electrons through gases. At the lower incident energies, the backward scattering is predominant, exhibiting a large MTCS. In contrast to the diverging nature of DCS in the forward direction (at the large

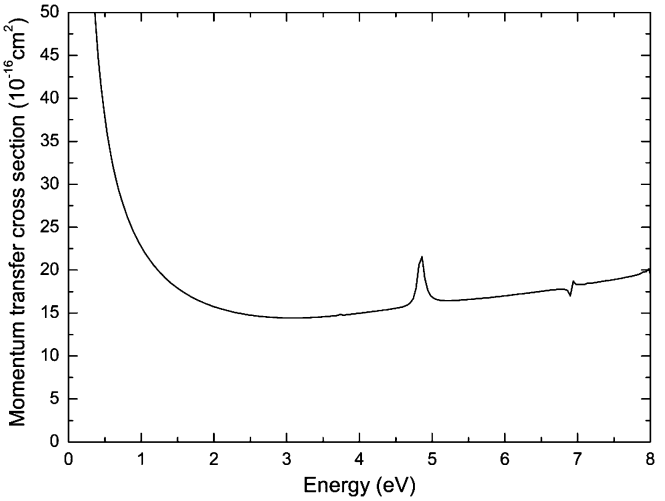

FIG. 7. Momentum transfer cross section in the energy range of 0.01–8.00 eV.

scattering angles), MTCSs show no singularity due to the multiplicative factor $(1 - \cos\theta)$, where θ is the scattering angle. The peak near 5 eV of the MTCS is basically due to the formation of the $^2B_1$ core-excited shape resonance, and the peak around 7 eV may arise from the $^2A_1$ Feshbach resonance. The resonance with $^2B_1$ symmetry is also observed in the elastic cross-section calculations as a small jump around 5 eV on the blue dash-dotted line in Fig. 1. Since the SCF orbitals of H_2CS^- are used for the $^2B_1$ symmetry elastic cross-section calculations, this resonance position observed in the elastic cross section shifts slightly to lower energy with respect to that observed in the excitation cross sections (Figs. 2–4). In Fig. 7, these two peaks show distinctly different shapes, implying the contrasting phase couplings between the resonant states and the background. If only one angular momentum l is essential for a certain resonance, the MTCS at the resonant position will be in the shape of the peak at ∼5 eV in Fig. 7 when the background phase shift (δ_{bg}) is zero. This type of resonance is often called a *pure* Breit-Wigner resonance. On the other hand, when $\delta_{bg} = 3\pi/4$, the peak shape is shown to be that at 7 eV in Fig. 7.

C. Stretching the C = S bond

The present study identifies two low-lying core-excited shape resonances at 3.62 and 5.15 eV in $^2B_2$ and $^2B_1$ symmetries, respectively. The first core-excited shape resonance $^2B_2$ is formed by trapping the scattering electron at the lowest unoccupied MO (LUMO) $3b_1$ and simultaneously promoting the target molecule (H_2CS) to the $1\ ^3A_2$ state; similarly, the promotion to the $1\ ^3A_1$ state of the target and the electron trapping at the LUMO lead to the second core-excited shape resonance $^2B_1$. These two core-excited shape resonances are unstable, especially for the second resonance due to its quite large resonance width. They could decay into their respective parent states by detachment of the trapped electron. Since the LUMO of H_2CS is an antibonding orbital $\pi_{C=S^*}$ as shown in the inset of Fig. 8, the full occupation of this orbital at these two resonance states could dramatically weaken the C=S bond. Therefore, the C=S bond cleavage is another vitally important decaying channel of H_2CS^- of these two resonant states. To explore the possible C=S bond dissociation coupling with these two resonant states, we perform a series of R-matrix calculations at these two resonant states, specifically by stretching the C=S bond length while fixing the CH bond length and the HCH bending angle at the equilibrium in C_{2v} symmetry.

As shown in Fig. 8, the resonance positions and widths of the $^2B_1$ and $^2B_2$ core-excited shape resonant states change gradually with the C=S bond stretching. When the C=S bond is elongated, the resonance positions and widths decrease as expected. This suggests that the C=S bond could be spontaneously broken and then produce the stable anionic and neutral fragments. Since the EA of the S atom [EA(S) = 2.08 eV [55] is much larger than that of CH_2 radical [EA(CH_2) = 0.652 eV [56], we conjecture that the fragments can be S^- and CH_2. Using the thermochemical data of H_2CS [30], CH_2, and S [57], we estimate that the dissociation energy D_0 of $e^- + H_2CS \rightarrow CH_2 + S^-$ is 3.57 eV. Since the position of the first

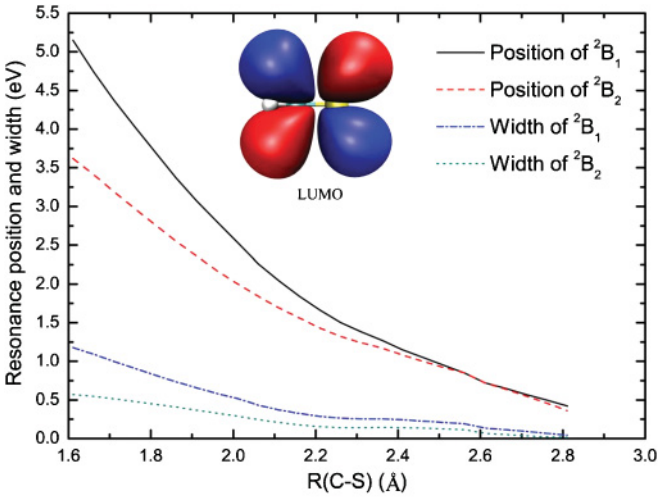

FIG. 8. (Color online) Variation of resonance position and width in terms of the different C-S bond length. Solid curve: position of $^2B_1$; dashed curve: position of $^2B_2$; dash-dotted curve: width of $^2B_1$; dotted curve: width of $^2B_2$. Inset: the lowest unoccupied molecular orbital (LUMO) $3b_1$ of H_2CS.

core-excited shape resonance $^2B_2$ is at 3.62 eV, the following channel is energetically permitted:

$$H_2CS^-(^2B_2) \rightarrow CH_2(X^3B_1) + S^-(^2P).$$

On the other hand, the adiabatic energies for the transitions from the ground state $X\ ^3B_1$ to the first two excited states $a\ ^1A_1$ and $b\ ^1B_1$ of CH_2 radical are 0.483 and 1.542 eV [58], respectively. The second core-excited shape resonance $^2B_1$ at 5.15 eV may couple with not only the above dissociation but also the following two channels:

$$\begin{aligned} H_2CS^-(^2B_1) &\rightarrow CH_2(a^1A_1) + S^-(^2P) \\ &\rightarrow CH_2(b^1B_1) + S^-(^2P) \end{aligned}$$

if we assume that the product S^- remains to be at its ground state. To the best of our knowledge, there is still no experimental report on the dissociative electron attachment to the H_2CS molecule.

Finally, we make a brief comparison between formaldehyde (H_2CO) and H_2CS. The electron impact with H_2CO was always studied with the R matrix [40], the complex Kohn variational [59], and the Schwinger multichannel [60] methods. The common points and the differences are addressed here: Since these two molecules have large dipole moments, the Born corrections to the elastic cross sections are important. A shape resonance of the $^2B_1$ symmetry was observed clearly both in the electron transmission experiments [61] and by the theoretical elastic cross-section calculations [40,59,60] for H_2CO; however, there are no distinct resonance peaks exhibited in the present theoretical elastic cross-section profile for H_2CS. In the inelastic-scattering calculations, some core-excited shape and Feshbach resonances are significant for H_2CS (see Figs. 2–4), while they are not distinctly observed for H_2CO (see Figs. 8–10 in Ref. [40]). As for the C = X (O,S) bond cleavage, only the shape-resonant ($^2B_1$) anion H_2CO^- was discussed [40], while two core-excited shape resonant states $^2B_2$ and $^2B_1$ are discussed for H_2CS^-, and

the neutral fragment CH_2 is proposed to be at three possible states, depending on the electron collision energies.

V. CONCLUSION

The elastic and excitation inelastic cross sections of the low-energy electron collision with the H_2CS molecule are calculated using the *R*-matrix method with an adequate target representation. For the low-lying excited states of the target, our results are in good agreement with the MR-CI calculation results [23–25]. The molecular properties at the ground state are also in accord with the experimental results [31,32,34]. The electron-scattering calculations show three core-excited shape resonant states $^2B_2$ (3.62 eV), $^2B_1$ (5.15 eV), and $^2A_1$ (7.98 eV) and three Feshbach resonant states $^2B_2$ (6.55 eV), $^2A_1$ (6.94 eV), and $^2B_1$ (9.05 eV). Due to the larger dipole moment of the target, the backward scattering is preferred for the elastic and inelastic scatterings. With the increase of the incident energy, one of the minima of the forward-scattering DCSs shifts to the smaller scattering angle. The configurations of the first two low-lying core-excited shape resonances $^2B_2$ and $^2B_1$ show the full occupation of the anti C=S bond orbital $3b_1$ (π^*), implying that the C=S bond may be weakened at these two resonant states. Our calculations indicate further that the C=S bond can be broken simply via the C=S bond stretching. Moreover, the $S^-(^2P)$ and CH_2 ($X\,^3B_1$, $a\,^1A_1$, and $b\,^1B_1$ states) fragments are proposed as the products of the dissociative electron attachments via the first two core-excited shape resonances.

ACKNOWLEDGMENTS

This work is partially supported by the Fundamental Research Funds for the Central Universities (Grant No. WK2340000012) and MOST (Grant No. 2011CB921401). Dr. S. B. Zhang is acknowledged for his kind help with the calculations.

[1] Y. C. Minh, W. M. Irvine, and M. K. Brewer, Astron. Astrophys. **244**, 181 (1991).
[2] K. Willacy and T. J. Millar, Astron. Astrophys. **324**, 237 (1997).
[3] S. D. Taylor, O. Morata, and D. A. Williams, Astron. Astrophys. **336**, 309 (1998).
[4] M. Agúndez, J. P. Fonfría, J. Cernicharo, J. R. Pardo, and M. Guélin, Astron. Astrophys. **479**, 493 (2008).
[5] J. I. Moses, M. Allen, and G. R. Gladstone, Geophys. Res. Lett. **22**, 1597 (1995).
[6] B. E. Turner, Astrophys. J. **468**, 694 (1996).
[7] K. Kasatani, M. Kawasaki, and H. Sato, Chem. Lett. **1**, 62 (2001).
[8] R. Flammang, D. Landu, S. Laurent, M. Barbieux-Flammang, C. O. Kappe, M. W. Wang, and C. Wentrup, J. Am. Chem. Soc. **116**, 2005 (1994).
[9] N. Tokiton, N. Takeda, and R. Okazaki, J. Am. Chem. Soc. **16**, 7907 (1994).
[10] T. Taketsugu and T. Hirano, J. Chem. Phys. **99**, 9860 (1993).
[11] R. I. Kaiser, W. Sun, and A. G. Suits, J. Chem. Phys. **106**, 5288 (1997).
[12] J. S. Kwiatkwski and L. Lenzczynski, J. Phys. Chem. **97**, 1845 (1993).
[13] J. R. Dunlop and D. J. Clouthier, J. Chem. Phys. **93**, 6371 (1990).
[14] P. Avouris, W. M. Gelbart, and M. A. El-Sayed, Chem. Rev. **77**, 793 (1977).
[15] R. I. Kaiser, C. Ochsenfeld, M. Head-Gordon, and Y. T. Lee, J. Chem. Phys. **110**, 239 (1999).
[16] R. H. Judge and G. W. King, Can. J. Phys. **53**, 1927 (1975).
[17] R. H. Judge, D. C. Moule, and G. W. King, J. Mol. Spectrosc. **81**, 37 (1980).
[18] R. H. Judge, C. R. Drury-Lessard, and D. C. Moule, Chem. Phys. Lett. **53**, 82 (1978).
[19] C. R. Drury, J. Y. K. Lai, and D. C. Moule, Chem. Phys. Lett. **87**, 520 (1982).
[20] C. R. Drury and D. C. Moule, J. Mol. Spectrosc. **92**, 469 (1982).
[21] S.-Y. Chiang and I.-F. Lin, J. Chem. Phys. **122**, 094301 (2005).
[22] H.-C. Wu, C.-C. Chen, and Y.-T. Chen, Spectrochim. Acta, Part A **69**, 27 (2008).
[23] P. J. Bruna, S. D. Peyerimhoff, R. J. Buenker, and P. Rosmus, Chem. Phys. **3**, 35 (1974).
[24] P. G. Burton and S. D. Peyerimhoff, Chem. Phys. **73**, 83 (1982).
[25] M. R. J. Hachey and F. Grein, Can. J. Phys. **73**, 18 (1995).
[26] M. R. J. Hachey and F. Grein, Chem. Phys. **197**, 61 (1995).
[27] M. R. J. Hachey and F. Grein, J. Mol. Spectrosc. **172**, 384 (1995).
[28] F. Grein and M. R. J. Hachey, Int. J. Quantum Chem. **30**, 1661 (1996).
[29] A. Jones and F. P. Lossing, J. Phys. Chem. **71**, 4111 (1967).
[30] B. Ruscic and J. Berkowitz, J. Chem. Phys. **98**, 2568 (1993).
[31] H. W. Kroto and R. J. Suffolk, Chem. Phys. Lett. **15**, 545 (1972).
[32] B. Solouki, P. Rosmus, and H. Bock, J. Am. Chem. Soc. **98**, 6054 (1976).
[33] S. Moran and G. B. Ellison, Int. J. Mass Spectrom. Ion Proc. **80**, 83 (1987).
[34] B. Fabricant, D. Krieger, and J. S. Muenter, J. Chem. Phys. **67**, 1576 (1977).
[35] D. R. Johnson, F. X. Powell, and W. H. Kirchhoff, J. Mol. Spectrosc. **39**, 136 (1971).
[36] L. A. Morgan, C. J. Gillan, J. Tennyson, and X. Chen, J. Phys. B **30**, 4087 (1997).
[37] L. A. Morgan, J. Tennyson, and C. J. Gillan, Comput. Phys. Commun. **114**, 120 (1998).
[38] H. Munjal, K. L. Baluja, and J. Tennyson, Phys. Rev. A **79**, 032712 (2009); J. S. Rajvanshi and K. L. Baluja, *ibid.* **81**, 022709 (2010); S. B. Zhang, J. G. Wang, R. K. Janev, and X. J. Chen, *ibid.* **82**, 062711 (2010).
[39] M. Gupta and K. L. Baluja, Eur. Phys. J. D **41**, 475 (2007); D. Bouchiha, J. D. Gorfinkiel, L. G. Caron, and L. Sanche, J. Phys. B **40**, 1259 (2007); S. Kaur and K. L. Baluja, Phys. Rev. A **82**, 022717 (2010).
[40] S. Kaur and K. L. Baluja, J. Phys. B **38**, 3917 (2005).
[41] N. Sanna and F. A. Gianturco, Comput. Phys. Commun. **114**, 142 (1998).

[42] P. G. Burke and K. A. Berrington, *Atomic and Molecular Processes: An R-matrix Approach* (Institute of Physics, Bristol, 1993).
[43] C. J. Gillan, J. Tennyson, and P. G. Burke, in *Computational Methods for Electron-Molecule Collisions*, edited by W. M. Huo and F. A. Gianturco (Plenum, New York, 1995).
[44] B. M. Nestmann, K. Pfingst, and S. D. Peyerimhoff, J. Phys. B **27**, 2297 (1994).
[45] D. R. Johnson, F. X. Powell, and W. H. Kirchhoff, J. Mol. Spectrosc. **39**, 136 (1971).
[46] T. H. Dunning and P. J. Hay, in *Methods of Electronic Structure Theory*, edited by H. F. Schaefer, Vol. 2 (Plenum, New York, 1977).
[47] G. C. Lie and E. Clementi, J. Chem. Phys. **60**, 1275 (1974).
[48] S.-W. Chiu, W.-K. Li, W.-B. Tzeng, and C.-Y. Ng, J. Chem. Phys. **97**, 6557 (1992).
[49] A. Faure, J. D. Gorfinkiel, L. A. Morgan, and J. Tennyson, Comput. Phys. Commun. **144**, 224 (2002).
[50] S.-I. Chu and A. Dalgarno, Phys. Rev. A **10**, 788 (1974).
[51] S. Kaur, K. L. Baluja, and J. Tennyson, Phys. Rev. A **77**, 032718 (2008).
[52] J. Tennyson and C. J. Noble, Comput. Phys. Commun. **33**, 421 (1984).
[53] H. Friedrich, in *Theoretical Atomic Physics*, 3rd ed. (Springer, Berlin, 2006), p. 47.
[54] F. A. Gianturco and A. Jain, Phys. Rep. **143**, 347 (1986).
[55] K. Rempala and K. M. Ervin, J. Chem. Phys. **112**, 4579 (2000).
[56] D. G. Leopold, K. K. Murray, A. E. Stevens Miller, and W. C. Lineberger, J. Chem. Phys. **83**, 4849 (1985).
[57] M. W. Chase Jr., J. Phys. Chem. Ref. Data Monogr. **9**, 1 (1998).
[58] C. D. Sherrill, M. L. Leininger, T. J. V. Huis, and H. F. Schaefer III, J. Chem. Phys. **108**, 1040 (1998).
[59] T. N. Rescigno, C. W. McCurdy, and B. I. Schneider, Phys. Rev. Lett. **63**, 248 (1989).
[60] T. C. Freitas, M. A. P. Lima, S. Canuto, and M. H. F. Bettega, Phys. Rev. A **80**, 062710 (2009).
[61] P. D. Burrow and J. A. Michejda, Chem. Phys. Lett. **42**, 223 (1976).